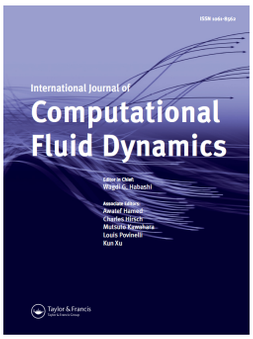

International Journal of Computational Fluid Dynamics

ISSN: 1061-8562 (Print) 1029-0257 (Online) Journal homepage: www.tandfonline.com/journals/gcfd20

A Numerical Investigation of Peristaltic Waves in Circular Tubes

Q. Xiao & M. Damodaran

To cite this article: Q. Xiao & M. Damodaran (2002) A Numerical Investigation of Peristaltic Waves in Circular Tubes, International Journal of Computational Fluid Dynamics, 16:3, 201-216, DOI: 10.1080/10618560290034681

To link to this article: https://doi.org/10.1080/10618560290034681

International Journal of Computational Fluid Dynamics, 2002 Vol. 16 (3), pp. 201–216

A Numerical Investigation of Peristaltic Waves in Circular Tubes

Q. XIAO and M. DAMODARAN*

Center for Advanced Numerical Engineering Simulations, Nanyang Technological University, Nanyang Avenue, Singapore, Singapore 639798

(Received 15 March 2001; Revised 1 October 2001; In final form 24 January 2002)

Peristaltic pumping is a process of fluid transport arising from the progressive waves, which travel along the walls of a flexible channel. It is a primary physiological transport mechanism that is inherent in many tubular organs of the human body such as the ureter, the gastro-intestinal tract, the urethra, and so on. Many studies exist in literature with the aim of understanding the characteristics of peristaltic flow under the assumption of low Reynolds number and infinitely long wavelength in a two-dimensional channel. However, peristaltic pumping is also the mechanism used in other industrial applications such as the blood pump for which the Reynolds number has a moderately high value. As studies concerning moderate to high Reynolds number flow in the circular tube are rare in literature, in the present study, the peristaltic flow of an incompressible fluid is numerically simulated using the finite volume method for solving the incompressible Navier–Stokes equations in primitive variable formulation by means of an infinite train of sinusoidal waves traveling along the wall of an axi-symmetric tube. The computational model presented in this work covers a wider range of Reynolds number (0.01–100), wave amplitude (0–0.8), and wavelength (0.01–0.4) than the those attempted in previous studies reported in literature and some new results pertaining to the distribution of velocity, pressure, wall shear stress for different peristaltic flow conditions characterizing flow at moderately higher Reynolds number have been obtained. The effect of the wave amplitude, wavelength, and Reynolds number on the "flow trapping" mechanism induced by peristalsis has also been investigated here for higher ranges of values of the parameters characterizing peristalsis.

Keywords: Peristaltic flow; Numerical flow modeling; Circular cylindrical tubes; Reynolds number

INTRODUCTION

Peristaltic flow is generated in a channel or a circular tube when a progressive wave travels along the wall. It is a primary transport mechanism inherent in many tubular organs of the human body such as the ureter, the gastro-intestinal tract, the urethra, etc. Many studies have been carried out for understanding the characteristics of the transport mechanism associated with peristaltic flow under the assumption of low Reynolds number and infinitely long wavelength such as by Shapiro *et al.* (1969) and Jaffrin and Shapiro (1971). However, peristaltic pumping is also the transport mechanism used in other industrial and medical applications such as the blood pump in which the Reynolds number has a moderately higher value. The investigation of peristaltic flow in circular tube in the moderate and high Reynolds number range is therefore important. The present study is therefore motivated by the fact that attempts to model peristaltic flow in the moderate to high Reynolds number range is relatively few.

The main difficulty encountered in modeling the flow in the range of moderate Reynolds number is the non-linearity caused by the interaction of the moving wall and the curvilinear flow field. The analytical works of Fung and Yih (1968) and Jaffrin (1973) for the flows in a two-dimensional channel have been carried out under various simplifying assumptions such as small amplitude wave, infinite wavelength, low Reynolds number, and time-mean flow rate. Numerical simulations of peristaltic flows have been reported by Brown and Hung (1977), Takabatake and Ayukawa (1982), Pozridikis (1987), Rathish Kumar and Naidu (1995). Studies of peristaltic flow in circular cylindrical tubes have been addressed by only a few researchers. Early theoretical works included those of Shapiro *et al.* (1969) and Yin and Fung (1969) with more or less limitations on the wave amplitude, wavelength for

*Corresponding author. E-mail: mdamodaran@ntu.edu.sg

ISSN 1061-8562 print/ISSN 1029-0257 online © 2002 Taylor & Francis Ltd
DOI: 10.1080/10618560290034681

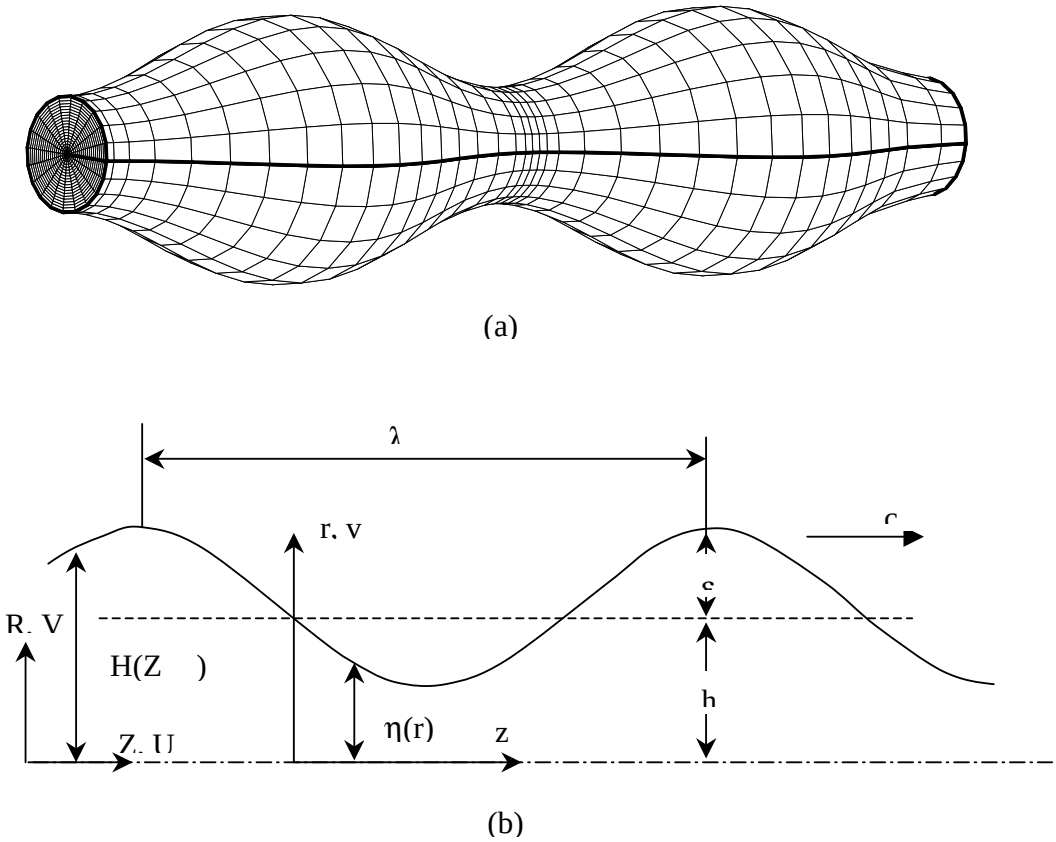

FIGURE 1 Configuration of peristaltic flow in two-dimensional axi-symmetric tube. (a) Typical orientation of wall shape during peristalsis (b) Definition of the parameters characterizing peristalsis.

lower Reynolds number. A numerical study based on the vorticity-stream function method has been conducted by Takabatake *et al.* (1988) in which the effect of Reynolds number and mean flow rate on the "trapping" phenomena has been investigated for a wave number of 0.01. As peristaltic flow in the circular tube or axi-symmetric case is more realistic than the two-dimensional channel and hence is worthy of further study from the point of view of physiological, medical, and general industrial applications.

In the present study, the peristaltic flow of an incompressible fluid by means of an infinite train of sinusoidal waves traveling along an axi-symmetric circular tube is numerically simulated using a finite volume method for solving the incompressible Navier–Stokes equations in primitive variable formulation and the approach differs from the earlier theoretical works and the study of Takabatake *et al.* (1988) in that the computational model presented in this study is extended to moderate Reynolds number (up to 100), wave amplitude, and wavelength. The study also focuses on the effect of the wave amplitude, wavelength, and Reynolds number on the flow structure. The simulation will also yield the velocity, pressure, wall shear stress distributions for different peristaltic flow conditions and enables the study of the influence of flow and geometry conditions on the strength and size of fluid "trapping."

In the following sections, the mathematical model and the numerical solution of these models are outlined briefly. This is followed by the verification of the method for two test cases and is followed by the discussion of the computed numerical results for the flow field, pressure distribution and wall shear stress in a circular tube with an infinite wavelength wave traveling along one wall. The conclusions will be made in the final section.

MATHEMATICAL MODELING AND NUMERICAL METHODS

The flow problem at hand is shown graphically in Fig. 1(a) and (b), which shows the propagation of an infinite sinusoidal wave train along the walls of an axi-symmetric tube in the axial direction defined in the fixed laboratory frame coordinates (Z, R). The peristaltic motion deforms the wall of the tube according to the equation:

$$H(Z,t) = h - \varepsilon \cos(2\pi/\lambda)(Z - ct) \qquad (1)$$

where t is the time, h is the mean distance of the wall from the symmetric axis, ϵ is the wave amplitude, λ is the wavelength and c is the wave speed.

In the fixed coordinate frame (Z, R) (the laboratory frame), the flow in the channel is unsteady because of the

moving boundary. However, the flow in the moving coordinate system (z, r) (the wave frame), which travels in the positive Z-direction with the same speed as the wave is steady. The transformation between the two frames are given by:

$$z = Z - ct \tag{2.1}$$

$$r = R \tag{2.2}$$

$$u(z, r) = U(Z - ct, R) - c \tag{2.3}$$

$$v(z, r) = V(Z - ct, R) \tag{2.4}$$

where (U, V) and (u, v) are the velocity components in the laboratory and the wave frame, respectively. In the present study, the flow will be treated as steady and solved in the wave frame. The flow structure in the laboratory frame will be derived from this steady solution by using the above relations.

In the wave frame, the integral forms of the continuity and Navier–Stokes equations take the following general forms:

$$\int_S \rho(\vec{v})\, \mathrm{d}\vec{S} = 0 \tag{3}$$

$$\int_S [\rho(\vec{v})v - \mathbf{T}]\, \mathrm{d}\vec{S} = \int_V S_v\, \mathrm{d}V \tag{4}$$

where $\mathbf{T}$ is the stress tensor.

The momentum conservation equation for the Cartesian velocity components u_i are as follows:

$$\int_S [\rho(\vec{v})u_i - t_i]\mathrm{d}\vec{S} = \int_V S_u\, \mathrm{d}V \tag{5}$$

where:

$$\begin{aligned} t_i &= \mathbf{T}\cdot i_i \\ &= -\left(p + \frac{2}{3}\mu \mathrm{div}\, v\right) i_i + \mu \mathrm{grad}\, u_i + \mu(\mathrm{grad} v)^{\mathbf{T}}\cdot i_i \end{aligned} \tag{6}$$

and μ denotes the dynamic viscosity of the fluid. In the wave frame, the shape of the peristaltic wall can be represented by:

$$\eta(z) = h - \varepsilon \cos(2\pi z/\lambda) \tag{7}$$

The boundary conditions for the wall $r = \eta(z)$ and the symmetric plane $r = 0$ can be expressed as follows:

$$\frac{\partial u}{\partial r} = 0, \quad v = 0 \text{ on } r = 0 \tag{8.1}$$

$$u = -c \quad v = -\frac{2\pi\varepsilon}{\lambda} c \sin\frac{2\pi z}{\lambda} \quad \text{on } r = \eta(z) \tag{8.2}$$

The flow rate q in the wave frame has the following relationship with the time-mean flow rate in the laboratory frame $\bar{Q}$:

$$\frac{q}{\pi h^2 c} = \frac{\bar{Q}}{\pi h^2 c} - (1 + 0.5\phi^2) \tag{9}$$

The non-dimensionless relative pressure is defined as:

$$\bar{p} = \frac{h^2}{\mu c \lambda}(p - p_{\mathrm{ref}}) \tag{10}$$

and the non-dimensional pressure rise along one wavelength is defined as:

$$\Delta\bar{p} = (h^2/4\mu c\lambda)(\Delta p_\lambda) \tag{11}$$

where p and Δp_λ is the dimensional pressure and pressure rise along one wavelength, respectively, while p_{ref} is the reference pressure at the point $z = r = 0$.

In order to make comparisions with the studies of Takabatake *et al.* (1988), an estimate of the stream function defined as:

$$u = -\frac{1}{r}\frac{\partial \psi}{\partial z} \quad v = \frac{1}{r}\frac{\partial \psi}{\partial r} \tag{12}$$

from the computed velocity fields is necessary. As both the planes $r = 0$ and $r = \eta(z)$ constitute the streamlines in the wave frame, the flow rate q in the wave frame is constant. The stream function at $r = 0$ and $r = \eta(z)$ satisfy the following equation.

$$\begin{aligned} &\psi = 0 \quad \text{on} \quad r = 0 \quad \text{and} \\ &\psi = \psi_{\mathrm{wall}} = q\,(= \text{constant}) \quad \text{on} \quad r = \eta(z) \end{aligned} \tag{13}$$

The problem of the peristaltic flow is controlled by four dimensionless parameters, namely the amplitude ratio $\phi = (\varepsilon/h)$, the wavenumber $\alpha = (h/\lambda)$, the Reynolds number $Re = (ch\alpha/\upsilon)$, which represents the ratio of inertial and viscous terms when peristalsis acts as a pump as described by Shapiro *et al.* (1969) and which also represents the ratio of radial vorticity diffusion time to the period of the wave and the dimensionless time-mean flow rate $\bar{Q}/\pi ch^2$. The estimation of these parameters and their inter-relationships from the computational simulation will assist in the characterisation of persitaltic flows in the moderate to higher ranges of Reynolds number.

The flow generated by an infinite train of peristaltic waves can be treated the same way as the periodic flow that appears in the central part of the finite computational region. The computational domain in the present study is shown in Fig. 2 as the finite region A-B-C-D-E-F with two waves in the wave frame. (two cycles). Periodic boundary conditions are imposed on the sections CD, FA as follows:

$$u_{\mathrm{AF}}(z, r) = u_{\mathrm{CD}}(z, r) = u_{\mathrm{BE}}(z, r) \tag{14.1}$$

$$v_{\mathrm{AF}}(z, r) = v_{\mathrm{CD}}(z, r) = v_{\mathrm{BE}}(z, r) \tag{14.2}$$

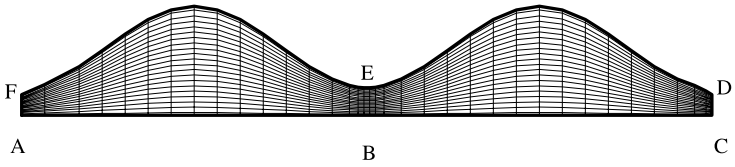

FIGURE 2 Computational domain and grid system.

The integral forms of the conservation Eqs. (3–6) are discretized on non-orthogonal grids using the finite volume approach and a collocated arrangement of variables on the computational grids. The typical control volume is shown in Fig. 3. The conservation equations can be written in the general form as follows:

$$\sum_j \int_{S_j} [\rho(\vec{V})\phi - \Gamma_\phi \mathrm{grad}\phi]\mathrm{d}\vec{S} = \int_V S_\phi \mathrm{d}V \qquad (15)$$

Equation (15) consists of three terms, namely the convective term ($\sum_j \int_{S_j}[\rho\phi\vec{V}]\mathrm{d}\vec{S}$), the diffusive term ($\sum_j \int_{S_j}[-\Gamma_\phi \mathrm{grad}\phi]\mathrm{d}S$) and the source terms ($\int_V S_\phi \,\mathrm{d}V$). The manner in which each of these terms are approximated for numerical implementation is outlined briefly below:

The convective term is expressed as:

$$\sum_j \int_{S_j} [\rho\phi\vec{V}]\mathrm{d}\vec{S} = [\rho\phi\vec{V}]_e\cdot\vec{\mathbf{S}}_e + [\rho\phi\vec{V}]_w\cdot\vec{\mathbf{S}}_w + [\rho\phi\vec{V}]_n\cdot\vec{\mathbf{S}}_n + [\rho\phi\vec{V}]_s\cdot\vec{\mathbf{S}}_s \qquad (16.1)$$

where $\vec{\mathbf{S}}_i$ $(i = e, w, n, s)$ is the surface vector. For the e side, which can be expressed as:

$$\vec{\mathbf{S}}_e = (y_{ne} - y_{se})\vec{\mathbf{i}} - (x_{ne} - x_{se})\vec{\mathbf{j}} \qquad (16.2)$$

The convective flux of a variable ϕ through the e face can be expressed as:

$$C_e = \int_{S_e} \rho\phi(\vec{V})\mathrm{d}\vec{S} \approx \rho_e\phi_e(\vec{V})\cdot\vec{S}_e \approx F_e\phi_e, \qquad (16.3)$$

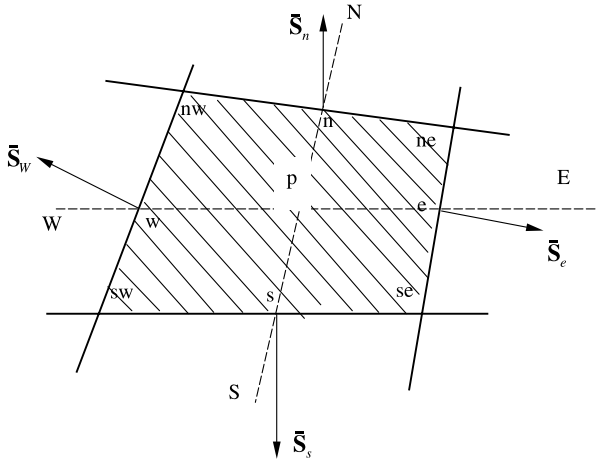

FIGURE 3 Sketch of control volume for numerical formulation.

In the above expressions, ϕ_e represents the cell face mean value of the variable ϕ, which should be obtained by the values from two neighbor grid points ϕ_E and ϕ_W. The convective flux $F_e\phi_e$ is approximated using "deferred correction" approach, which is the combination of the second-order central differencing scheme (CDS) and first-order upwind differencing (UDS):

$$(F\phi)_e = (F\phi)_e^{\mathrm{UDS}} + \gamma[(F\phi)_e^{\mathrm{UDS}} - (F\phi)_e^{\mathrm{UDS}}] \qquad (16.4)$$

where $\gamma(0 \le \gamma \le 1)$ is a factor allows the introduction of numerical diffusion which can be used to control the stability of the numerical scheme.

The diffusive fluxes through the e cell face can be approximated as follows: (see Demirdzic and Peric (1990) for details)

$$D_e = -\int_{S_e} \Gamma_\phi \mathrm{grad}\phi\,\mathrm{d}\vec{\mathbf{S}} \approx -\left[\frac{\Gamma_\phi}{V}\right]_e [(\phi_E - \phi_P)(\vec{\mathbf{S}}_e\cdot\vec{\mathbf{S}}_e) + (\phi_n - \phi_s) \times (\vec{\mathbf{S}}_e\cdot\vec{\mathbf{S}}_n)]_e \qquad (17)$$

The source term is integrated over the cell volume. By assuming that the specific source is defined at the control volume center and that it represents the mean value over the whole control volume, this term can be approximated as follows:

$$S_\phi = \int_V S_\phi \,\mathrm{d}V \approx (S_\phi)_P V \qquad (18)$$

The application of these approximations to each control volume or grid cell in the discretized flow field and the assembly of the fluxes through all the faces of one control volume results in a system of algebraic equations which links the value of the dependent variable at the center of each control volume with those in the neighboring control volumes as follows:

$$\phi_P = \frac{B_E^\phi\phi_E + B_W^\phi\phi_W + B_N^\phi\phi_N + B_S^\phi\phi_S + Q_P}{B_P^\phi} \qquad (19)$$

where the Bs are the coefficients containing contributions from diffusion and convection terms. The B_P^ϕ term is the sum of all the other Bs and the contribution from unsteady term. Q_P is the source terms containing all terms that are treated as explicit.

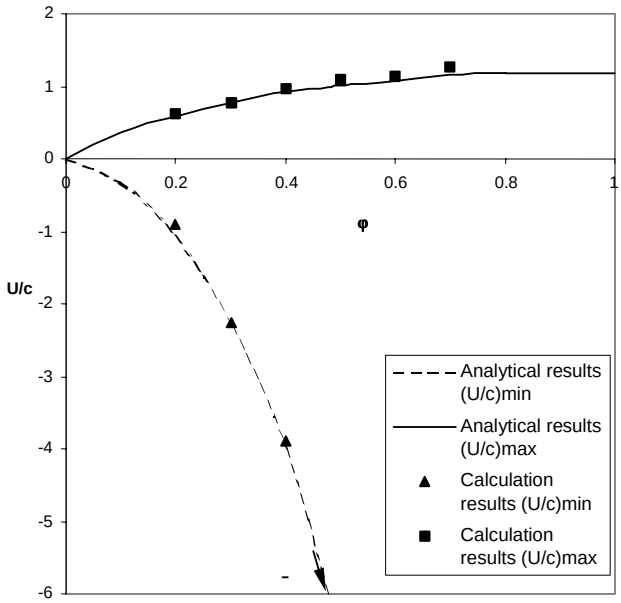

FIGURE 4 The comparison of the maximum and minimum axial velocity (U/c) predicted by present computation and analytical result with $\alpha = 0.01$ and $Re = 0.01$.

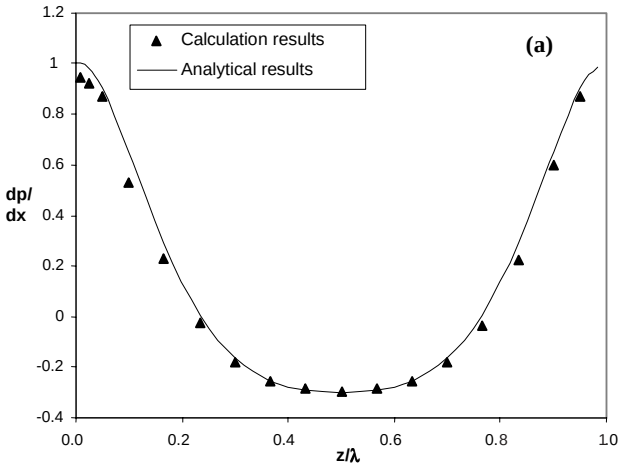

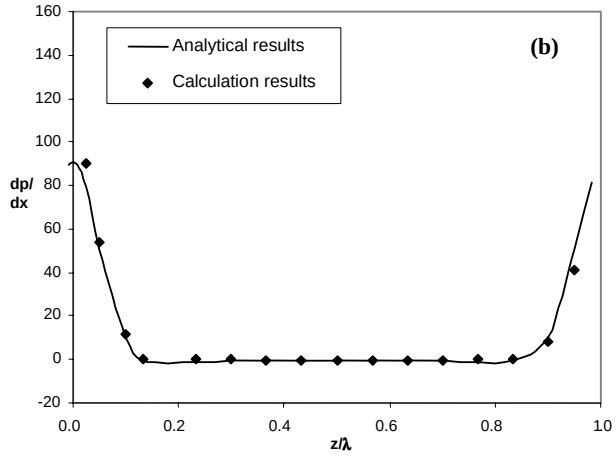

FIGURE 5 Comparison of computed results with theoretical results on the pressure gradient distribution for $Re = 0.01$, $\alpha = 0.01$, and $\bar{Q}/\pi ch^2 = 0$ (a) $\phi = 0.2$ (b) $\phi = 0.7$.

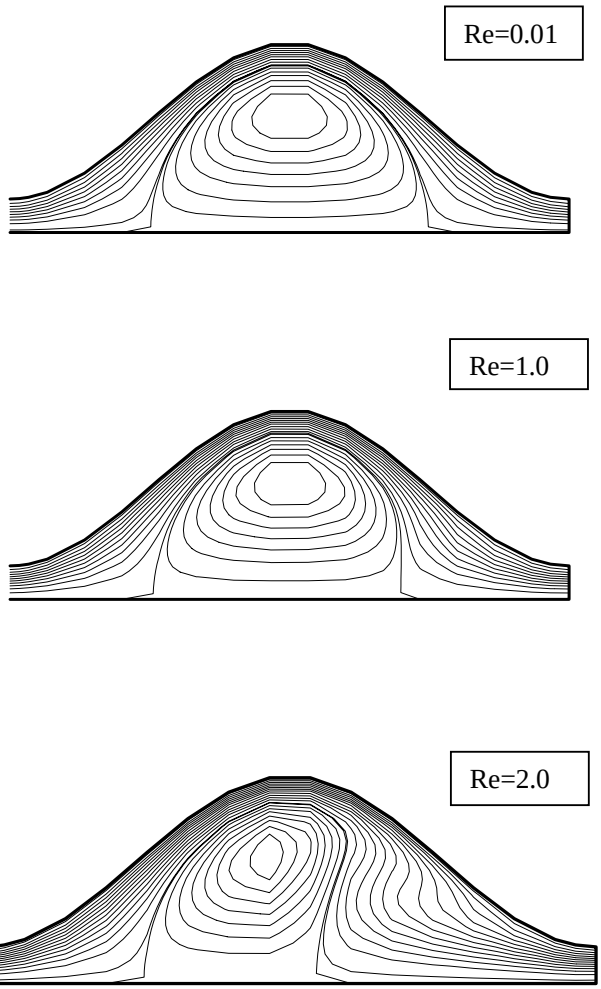

FIGURE 6 The effect of Reynolds number on the streamline patterns in the wave frame for $\alpha = 0.01$, $\varphi = 0.7$, $\bar{Q}/\pi ch^2 = 0.6$.

The strongly implicit procedure (SIP) based on an incomplete LU factorization of the coefficient matrix, is used for solving the unknowns. The pressure–velocity coupling is achieved using the well-known semi-implicit

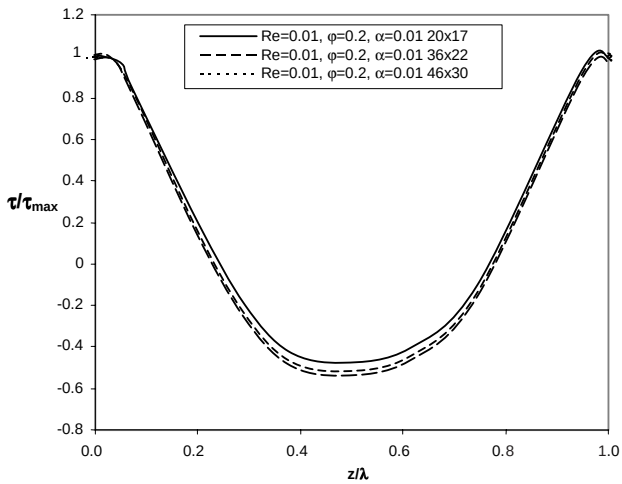

FIGURE 7 Grid dependence studies on three set of grids.

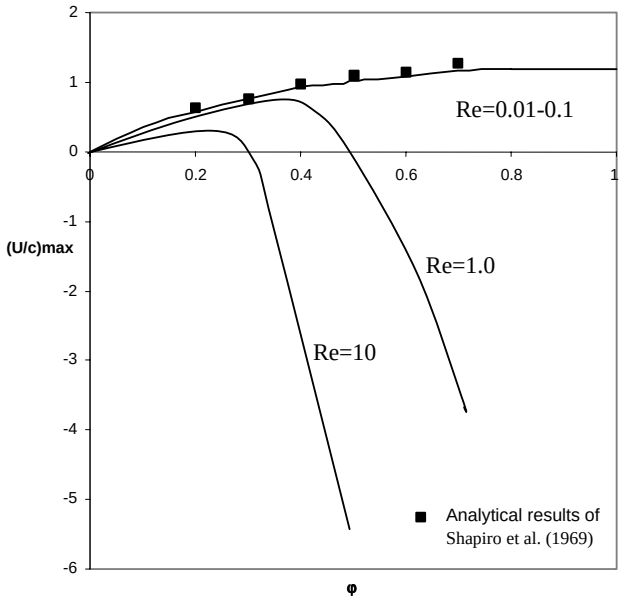

FIGURE 8 The effect of Reynolds number on the $(U/c)_{\max}$ of the axis for $\alpha = 0.01$, $\bar{Q}/\pi ch^2 = 0$ and different values of φ.

pressure linked explicit algorithm (SIMPLE) of Patankar and Spalding (1972). Special care is required for using a collocated variable arrangement to avoid pressure–velocity decoupling.

The computational procedure for the implementation of inflow and outflow boundary conditions is outlined as follows. At the initial stage of the iteration, prescribed values are specified at the inlet (FA) whereas at the outflow boundary (CD), derivatives of the properties with respect to the stream-wise direction are set zero. The iterative procedure is repeated until the mass residual source term decreases and becomes sufficiently small (for example less than 4% of the total mass). Then the periodic boundary condition is implemented by replacing the field data at the inlet (FA) with the computed solutions at the pertinent position (BE) in each iteration step. Periodicity is checked by comparing the computed data between the outlet (CD) and the same position at the location (BE). The computation is terminated when the periodicity in the flow is attained and is determined by the criteria when the mass residual source became much less than 1% of the total mass and also by observing the flow behavior.

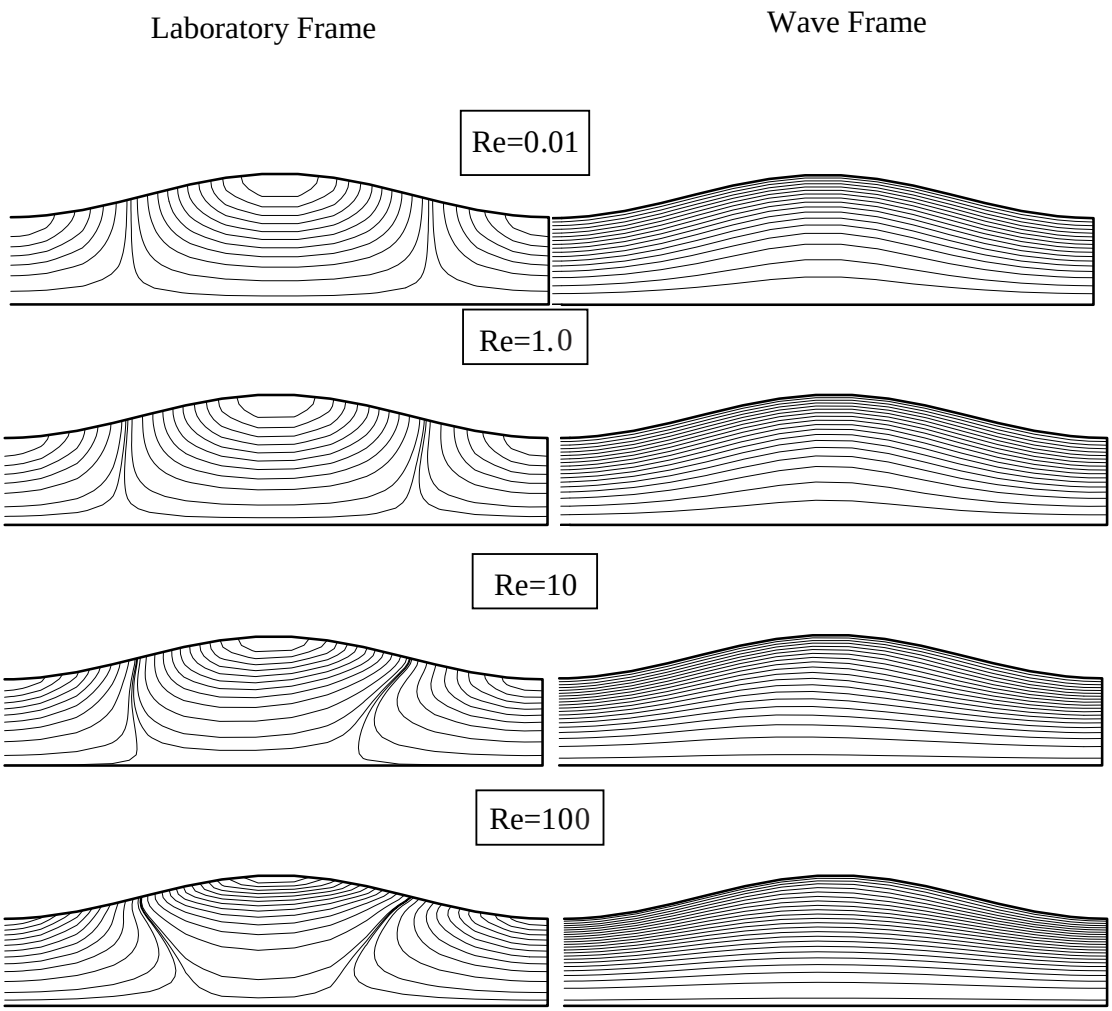

FIGURE 9(a) The effect of Reynolds number on the streamline patterns in the wave frame and laboratory frame for $\alpha = 0.01$, $\bar{Q}/\pi ch^2 = 0$. $\varphi = 0.2$.

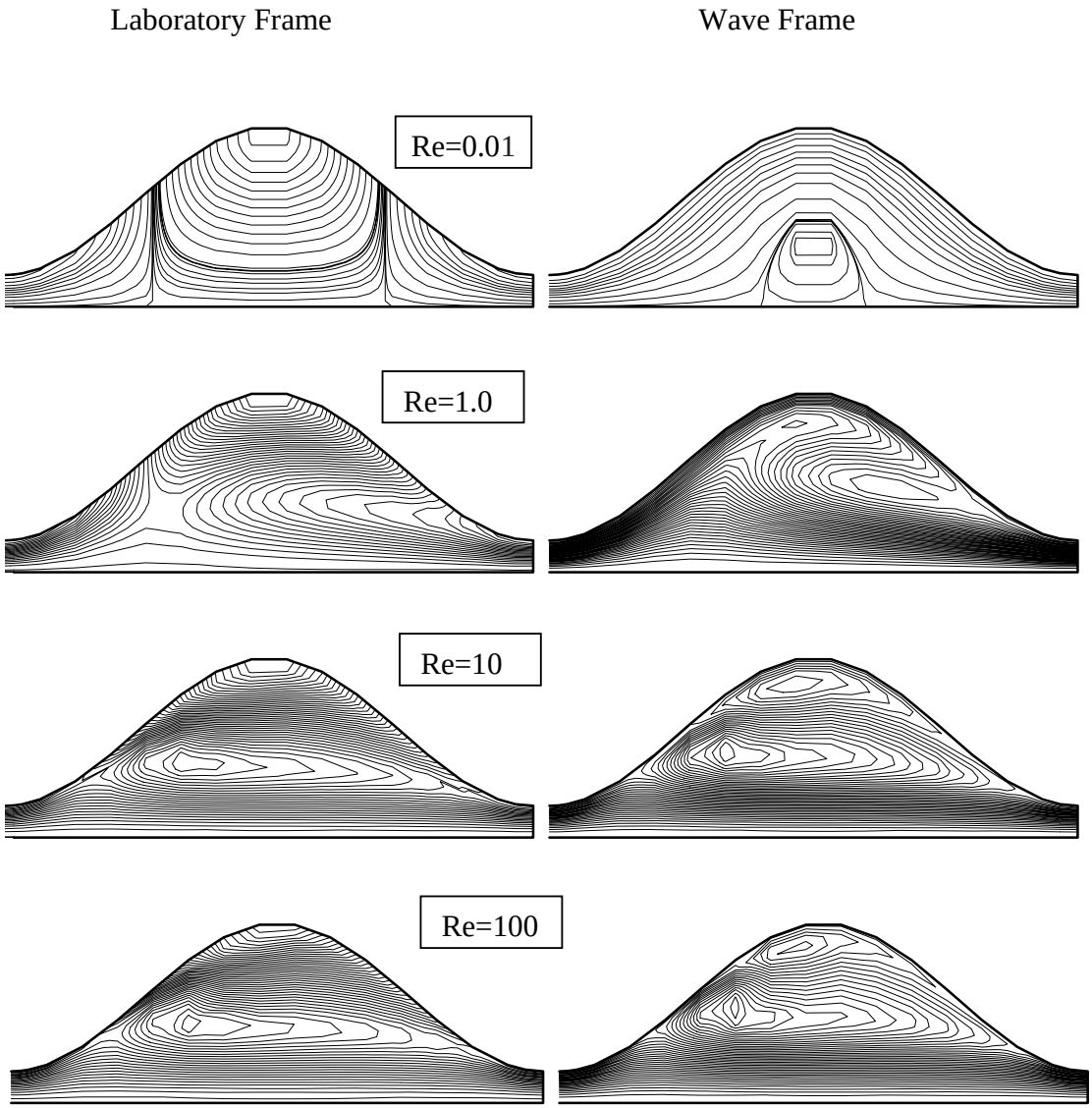

FIGURE 9(b) The effect of Reynolds number on the streamline patterns in the wave frame and laboratory frame for $\alpha = 0.01$, $\bar{Q}/\pi ch^2 = 0$. $\varphi = 0.7$.

RESULTS AND DISCUSSIONS

A couple of standard test problems are simulated for the purpose of verifying the numerical algorithm. The first problem considered here is the peristaltic flow through a two-dimensional axi-symmetric tube under the flow condition of $Re = 0.01$, and $\alpha = 0.01$ which is used to simulate the inertial free, long wavelength flow (i.e. $Re \rightarrow 0$, $\alpha \rightarrow 0$). The calculated maximum and minimum velocity at the crest and trough at the axis are compared with the theoretical results of Shapiro *et al.* (1969) in Fig. 4. In Fig. 5(a) and (b), the pressure gradient distribution for the wave amplitude $\varphi = 0.2$ and 0.7 are displayed together with Shapiro *et al.* (1969)'s results. It is clear from both figures that the present results are in good agreement with the theoretical results. Hence it is confirmed that the present code is valid with the flow condition of $Re = 0.01$, and $\alpha = 0.01$.

The second problem considered here is the finite Reynolds number case. Figure 6 shows the computed streamlines corresponding to $\varphi = 0.7$, $\bar{Q}/\pi ch^2 = 0.6$, and with the Reynolds number varying in the range from 0.01 to 2. The comparison with the numerical results of Takabatake *et al.* (1988) shows a fairly good agreement.

In order to assess the effects of grid dependence on the numerical solution, computations are conducted on three sets of grids, i.e. 20×17, 36×22, and 46×32 cell meshes. Figure 7 compares the computed normalized wall shear stress variation in the axial direction obtained by using the numerical method on these three grids and shows the effect of grid size on the computed results. As the differences are negligible between the results computed on the grids of size 36×22 and 46×32, most of the computations reported from this point onwards are done using the 36×22 grid size. Computational studies pertaining to the influence of Reynolds number and non-dimensional wavelength α on the flow field, pressure distribution and shear stress distribution along the wall are presented first based on the mean flow rate $\bar{Q}/\pi ch^2 = 0$

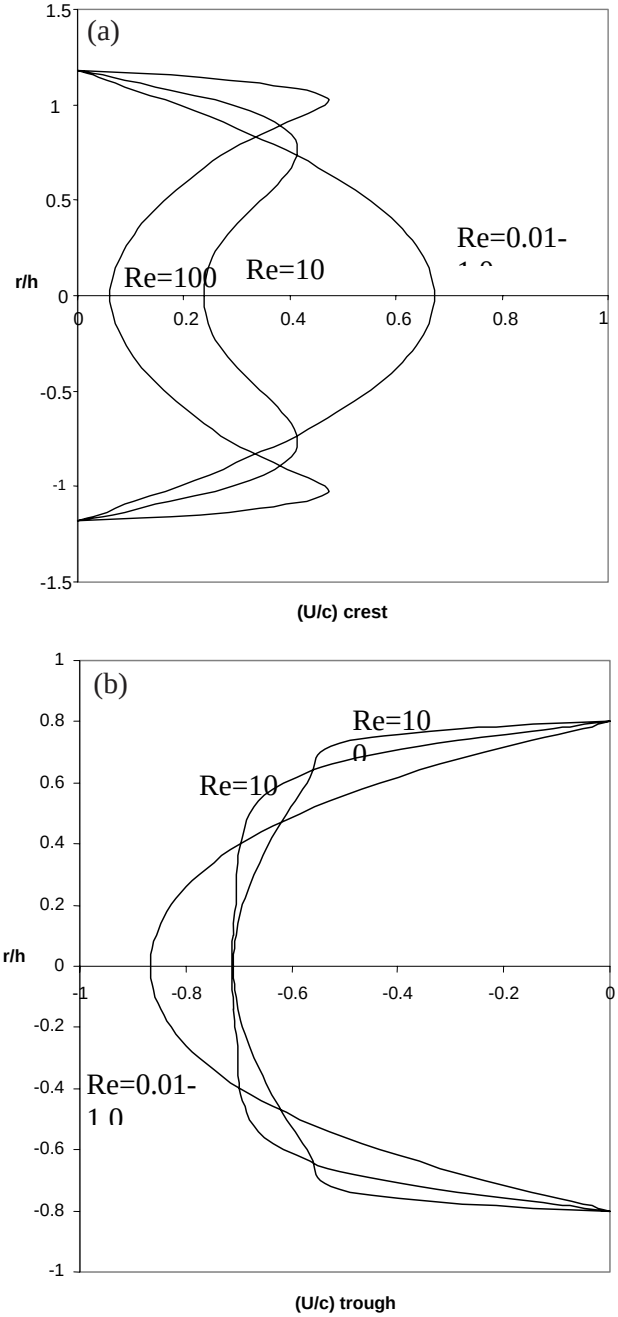

FIGURE 10 The effect of Reynolds number on the velocity profiles in the laboratory frame for $\varphi = 0.2$, $\alpha = 0.01$ and $\bar{Q}/\pi ch^2 = 0$. (a) wave crest (b) wave trough.

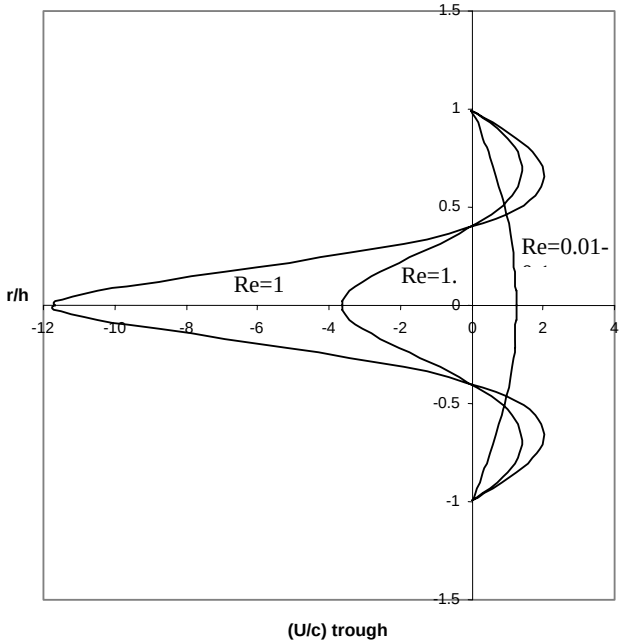

FIGURE 11 The effect of Reynolds number on the velocity profiles at wave trough in the laboratory frame. $\varphi = 0.7$, $\alpha = 0.01$ and $\bar{Q}/\pi ch^2 = 0$.

and followed by the computational studies focusing on the effect of *Re* and α on the fluid "trapping" phenomena.

Flow Structure, Pressure, Shear Stress Distribution for $\bar{Q}/\pi ch^2 = 0$

Reynolds Number Effect Corresponding the Case when $\alpha = 0.01$

Here computational results pertaining to the Reynolds number effect on the flow structure will be presented for the case corresponding to the geometric condition of $\alpha = 0.01$. Figure 8 shows the variation of the maximum normalized axial velocity $(U/c)_{\max}$ in the laboratory frame with φ for the range of $Re = 0.01$–10, $\bar{Q}/\pi ch^2 = 0$ and $\alpha = 0.01$. The corresponding results from the simplified analytical studies of Shapiro *et al.* (1969) evaluated for the low $Re = 0.01$ are also shown on this graph for comparison purposes. It can be seen from Fig. 8 that for the range of $Re = 0.01$–0.1, the present computed results based on the complete numerical model are in good agreement with the theoretical results of Shapiro *et al.* (1969) for the flow condition as $Re \to 0$, $\alpha \to 0$. This phenomena implies that within the range of $0.01 \leq Re \leq 0.1$, the Reynolds number effect (or the inertial force effect) on the $(U/c)_{\max}$ can be ignored within the limits of the numerical error associated with the numerical approximation. The effect of further increases in *Re* on the variation of maximum axial velocity with respect to φ can be seen from this figure as well. Figure 8 shows that for $\varphi < 0.3$, $(U/c)_{\max}$ increases with φ for all the *Re* under investigation (0.01–10). However, when φ is increased beyond 0.3, $(U/c)_{\max}$ for $Re = 10$ starts to decrease sharply with φ. A similar variation can be observed for $Re = 1.0$ with a delayed turning point at around $\varphi = 0.4$ where the decreasing trend starts.

Figure 9(a) and (b) shows the variation of the computed streamlines with the Reynolds number in both the wave frame and laboratory frame for $\alpha = 0.01$, $\bar{Q}/\pi ch^2 = 0$, $\varphi = 0.2$ and $\varphi = 0.7$, respectively. By comparing these two figures, the influence of Reynolds number on the flow structure can be observed and the effect is felt more for the case corresponding to $\varphi = 0.7$ than for the case corresponding to $\varphi = 0.2$. This result implies that the

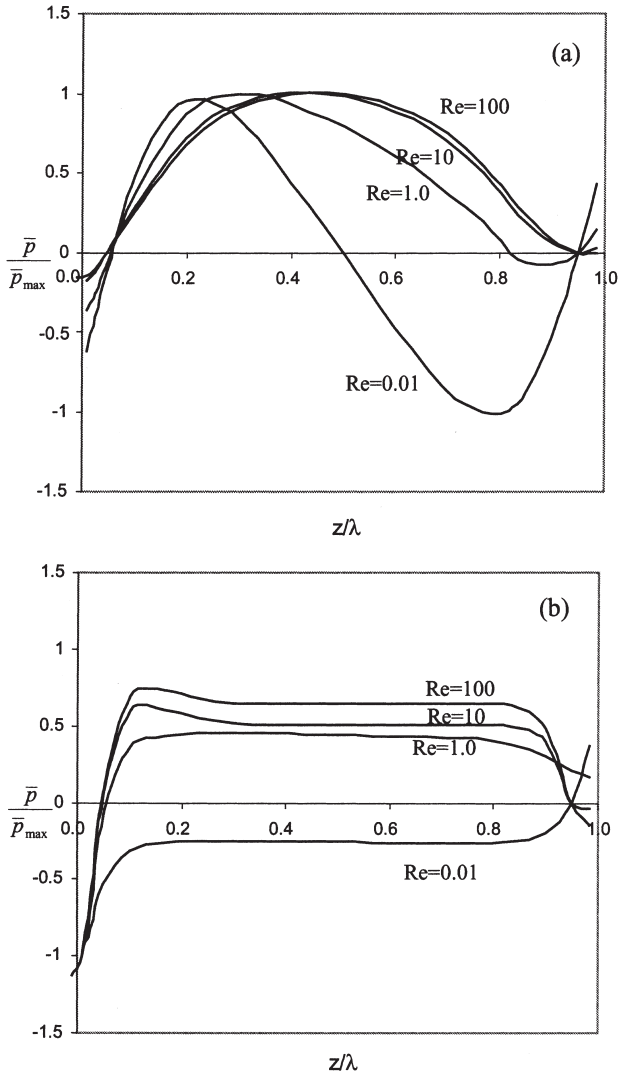

FIGURE 12 The effect of Reynolds number on the normalized pressure distribution for $\alpha = 0.01$ and $\bar{Q}/\pi ch^2 = 0$. (a) $\varphi = 0.2$ (b) $\varphi = 0.7$.

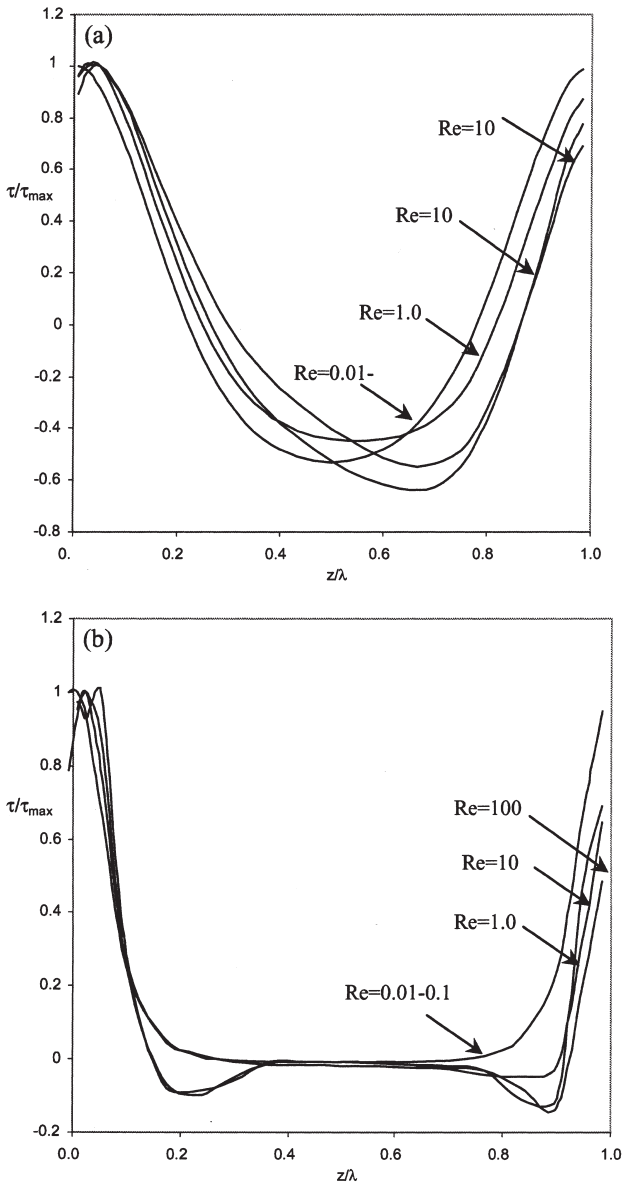

FIGURE 13 The effect of Reynolds number on the shear stress distribution for $\alpha = 0.01$ and $\bar{Q}/\pi ch^2 = 0$. (a) $\varphi = 0.2$ (b) $\varphi = 0.7$.

inertial force effect on the peristaltic flow is stronger for the case with a larger amplitude ratio.

In order to understand more details of the computed velocity fields, the variation of the velocity profiles in the tube at the crest and trough (in the laboratory frame) with the Reynolds number are shown, respectively, in Fig. 10(a) and (b) for $\varphi = 0.2$. The corresponding variation of the velocity profiles in the tube at the wave trough for $\varphi = 0.7$ are shown in Fig. 11. In these figures, the ordinate is the dimensionless coordinate r/h while the abscissa is U/c defined in the laboratory frame. It can be seen that, in the range of $0.01 < Re < 0.1$, both the velocity profiles at the crest and trough are nearly parabolic, which is in agreement with the asymptotic solution obtained by Shapiro *et al.* (1969) for $Re \to 0$, $\alpha \to \infty$. On the other hand, when the Reynolds number increases to $Re = 1.0$ for $\varphi = 0.7$ and $Re = 10$ for $\varphi = 0.2$, the velocity profile deviates from the parabolic shape and hence implies the existence of flow separation with the reversed velocity.

Figure 12(a) and (b) shows the Reynolds number effect on the normalized non-dimensional pressure distribution corresponding to flow cases where the amplitude ratio $\varphi = 0.2$ and 0.7, respectively, and for which $\bar{Q}/\pi ch^2 = 0$. It can be seen that the amplitude ratio has a strong effect on the pressure distribution. For $\varphi = 0.7$, the pressure distribution remains a constant in the central part of one wavelength (i.e. $0.2 < z/\lambda < 0.8$) with the sudden rise in $\bar{p}$ near the two boundaries of the wave cycle. However, for $\varphi = 0.2$, the pressure distribution varies with the z/λ during the whole wave cycle, and as Reynolds number increases the maximum non-dimensional pressure approaches the middle point of the wave cycle, i.e. $z/\lambda = 0.5$. One possible explanation is that for the large amplitude ratio, the difference in velocity between the central and two ends ($z/\lambda = 0$, and 1.0) is larger than the

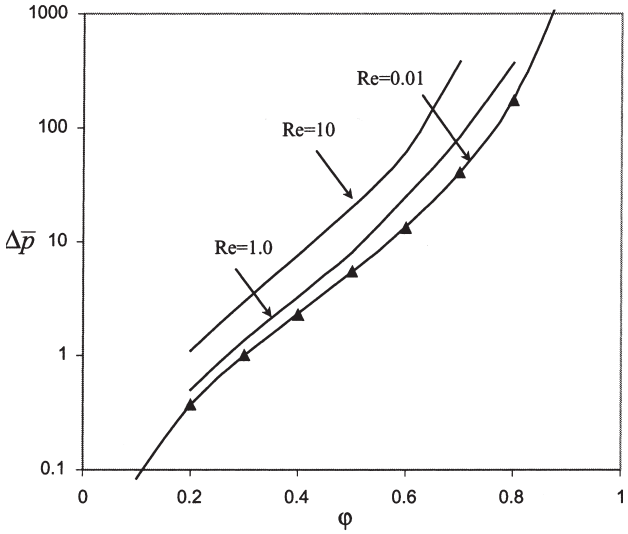

FIGURE 14 The effect of Reynolds number on the dimensionless pressure rise and dimensionless wave amplitude $\varphi(\alpha = 0.01)$.

corresponding small amplitude ratio, which results in the sudden pressure variation taking place at the locations of the two ends of the wave cycle.

The variation of the non-dimensional shear stress $(\tau/\tau_{\max})$ distribution along the peristaltic wall corresponding to

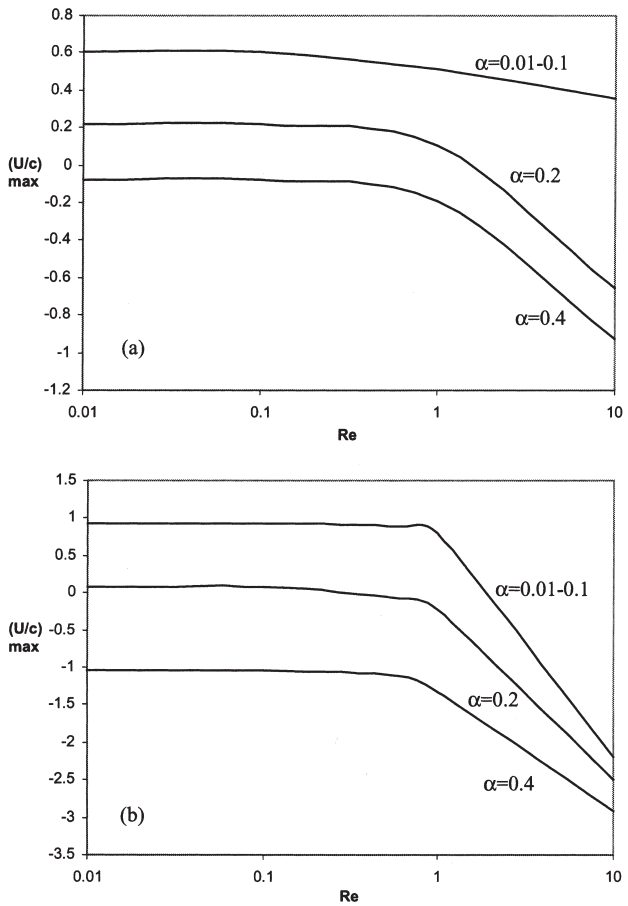

FIGURE 15 The effect of Reynolds number on the maximum axial velocity for different α. (a) $\varphi = 0.2$ (b) $\varphi = 0.4$.

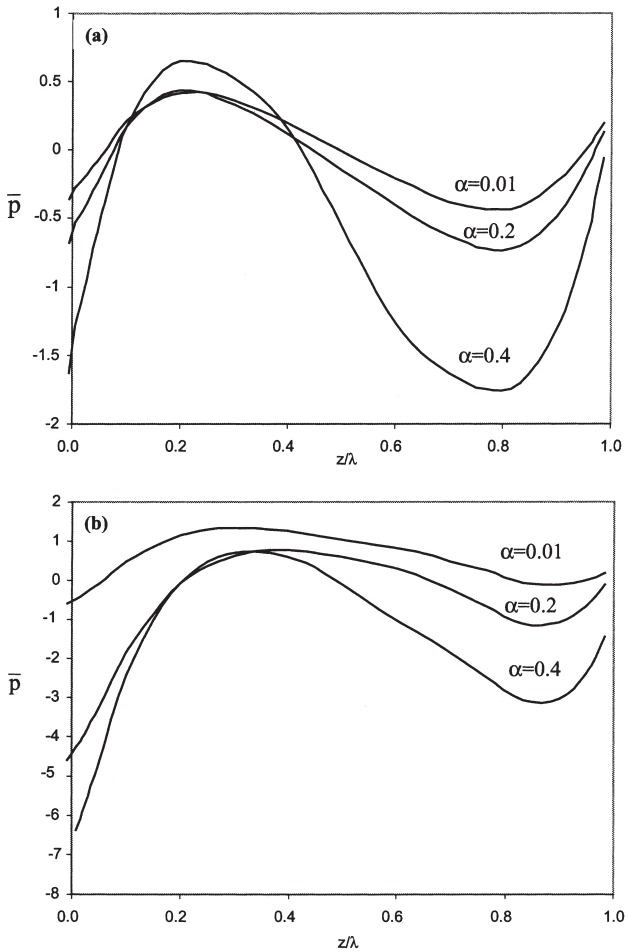

FIGURE 16 The effect of α on the pressure distribution for $\varphi = 0.2$. (a) $Re = 0.01$, (b) $Re = 1.0$.

the two cases $\varphi = 0.2$ and 0.7 are shown, respectively, in Fig. 13(a) and (b). It can be seen that for the range of Reynolds number Re from 0.01 to 1.0, the Reynolds number effect on the shear stress distribution is small for both cases although the variation of shear stress is much sharper for $\varphi = 0.2$ than $\varphi = 0.7$. Both figures show a symmetric feature about the midsection. In contrast, when the Reynolds number is increased further to $Re =$ 10 and 100, the symmetric feature is broken for $\varphi = 0.2$, and the location for the minimum shear stress moves downstream. For $\varphi = 0.7$, although the symmetric is maintained for the entire range, two locations for minimum shear stress appear around $z/\lambda = 0.2$ and 0.9.

Figure 14 shows the Reynolds number effect on the relationship between the dimensionless pressure rise for zero flow rate $(\bar{Q}/\pi ch^2 = 0)$ and the non-dimensional wave amplitude for $\alpha = 0.01$ predicted by the computational model and compared with analytical results of Shapiro *et al.* (1969) with $\alpha \to 0$ and $Re \to 0$. It can be seen that the results agree well. The figure also shows the Reynolds number effect on the rise of the dimensionless pressure as Reynolds number is increased while keeping φ fixed.

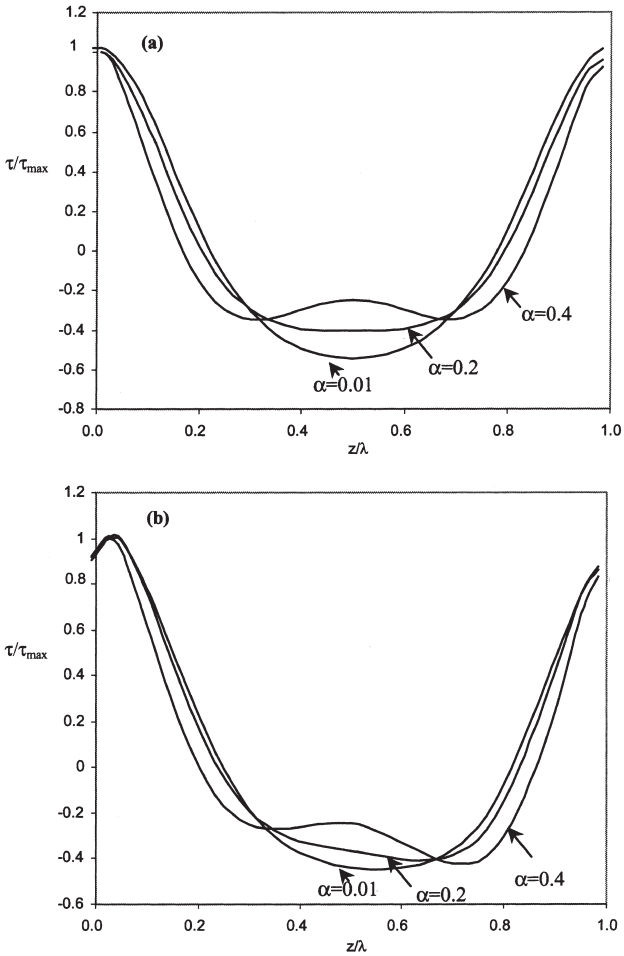

FIGURE 17 The effect of α on the shear stress distribution for $\varphi = 0.7$ (a) $Re = 0.01$, (b) $Re = 1.0$.

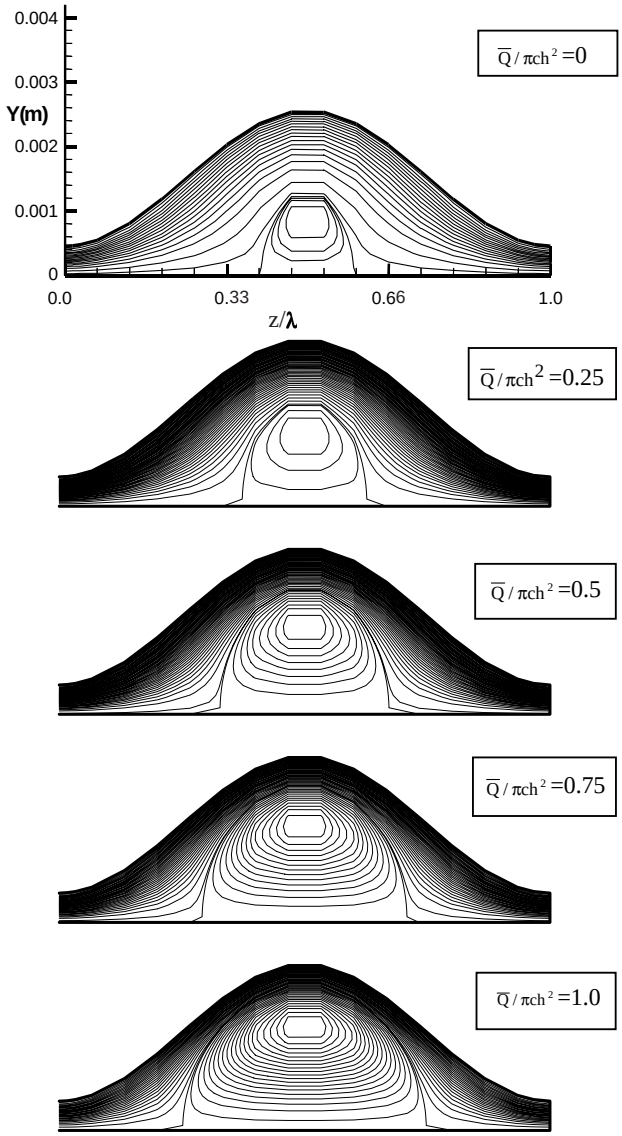

FIGURE 18 The streamline variation with $\bar{Q}/\pi ch^2$ (in the wave frame) for $\varphi = 0.7$, $\alpha = 0.01$, $Re = 0.01$.

Reynolds Number Effect Corresponding to the Case when $\alpha \gg 0.01$

In order to investigate the Reynolds number effect on the flow structure by relaxing the assumption of $\alpha = 0.01$, computations for cases when $\alpha = 0.1$, 0.2 and 0.4 are done. The computed results show that, for α less than 0.1, there are no significant variations or differences in the above distribution of the velocity field, pressure field and shear stress field. However, differences start to show when $\alpha \gg 0.01$.

The Reynolds number effect on the maximum axial velocity in the laboratory frame for different values $\alpha \gg 0.01$ corresponding to $\varphi = 0.2$, and $\varphi = 0.4$ are shown in Fig. 15(a) and (b), respectively. It can be seen from both figures that the variation of the maximum axial velocity $(U/c)_{\max}$ with Reynolds number show a similar trend. When $Re < 1.0$, $(U/c)_{\max}$ remains a constant (which is a function of α) irrespective of the Reynolds number. However, when $Re > 1.0$, $(U/c)_{\max}$ decreases with Reynolds number. The difference between Fig. 16(a) and (b)lies in the magnitude of $(U/c)_{\max}$, i.e. the absolute value of $(U/c)_{\max}$ for the case when $\varphi = 0.4$ is larger than the corresponding values for the case when $\varphi = 0.2$. Regarding the effect of variation in α on the value of $(U/c)_{\max}$, both figures show the decrease of $(U/c)_{\max}$ with α at the same Reynolds number.

Figure 16(a) and (b) shows the non-dimensional wavelength α effect on the pressure distribution along the wall for amplitude ratio $\varphi = 0.2$ at $Re = 0.01$ and $Re = 1.0$, respectively. It can be seen from both figures that, for a fixed Re, the variation in the pressure distribution during one wavelength increases as α increases. With regard to the Reynolds number effect on the pressure distribution, Fig. 16(a) shows that it is nearly symmetric about the central section (i.e. $z/\lambda = 0.5$) for $Re = 0.01$. However, this symmetric feature is broken for $Re = 1.0$ shown in Fig. 16(b). This implies that the influence of inertial effects on the flow field increases with the Reynolds number.

The effect of the non-dimensional wavelength α on the shear stress distribution are shown in Fig. 17(a) and (b),

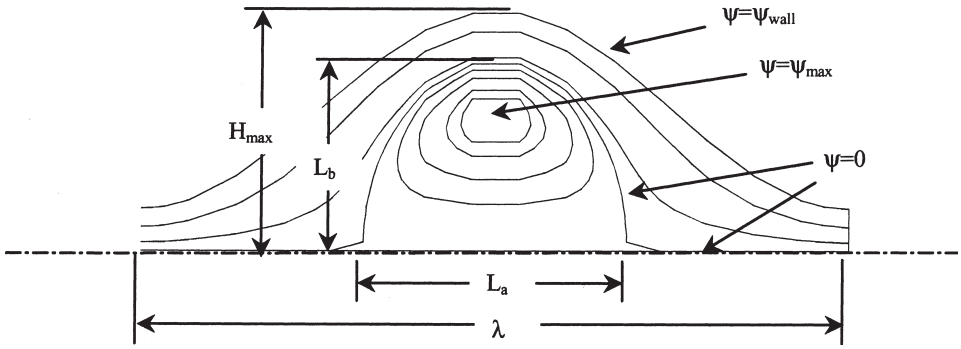

FIGURE 19 A schematic drawing for definition of flow trapping mechanism in peristalsis.

respectively for $Re = 0.01$ and 1.0 for the case when $\varphi = 0.7$. It can be seen that for both $Re = 0.01$ and $Re = 1.0$, as α increases the variation of shear stress, z/λ becomes more pronounced. For a given α, the variation in Reynolds number also affects the shear stress distribution. As Re increases the symmetric distribution which appear in Fig. 17(a) is broken in Fig. 17(b) for $\alpha \geq 0.2$.

Fluid Trapping in Peristaltic Flows

As computational studies discussed in the previous section are based on the mean flow rate $\bar{Q}/\pi ch^2 = 0$, in this section computational results are presented and discussed for the case when $\bar{Q}/\pi ch^2 \neq 0$. It has been known that for certain values of φ and $\bar{Q}/\pi ch^2$, a part of the fluid in the tube is enclosed by a streamline separated from the axis in the wave frame. The fluid moves forward with a net velocity equal to the wave speed in the laboratory frame as if it were trapped by the wave. This phenomenon is called "trapping". Previous studies on trapping in the circular tube are based on the assumption of either infinite long wavelength, i.e. $\alpha \rightarrow 0$ (Takabatake *et al.*, 1988; Shapiro *et al.*, 1969) or inertial free flow, i.e. $Re \rightarrow 0$ (Shapiro *et al.*, 1969). In the current study, the numerical investigation is extended to larger non-dimensional wavelength (i.e. $\alpha = 0.2, 0.4$) and for moderate Reynolds number ($0.01 < Re < 10$). For clarification, purposed focus will be made on the computational results obtained for the case when $\varphi = 0.7$ will be presented.

Trapping Corresponding to Re = 0.01

Figure 18 shows how the computed streamline flow patterns vary with different values of $\bar{Q}/\pi ch^2$ for the case when $\varphi = 0.7$, $\alpha = 0.01$ and $Re = 0.01$. It can be seen that for this particular value of φ, α and Re, there is a "trapping" phenomena occurring for a wide range of mean flow rate. ($0 \leq \bar{Q}/\pi ch^2 \leq 1.0$). It can also be seen that the size of the region of "trapping" increases as the value of $\bar{Q}/\pi ch^2$ increases. In order to quantify this phenomena of "trapping", three non-dimensional parameters defined by Takabatake *et al.* (1988), namely the two trapping lengths (L_a/λ), $(L_b/H_{\max})$, and the relative trapping intensity $|\psi_{\max}/\psi_{\text{wall}}|$ have been tracked during the course of the computation. Figure 19 is a schematic showing the significance of these parameters and how these are estimated from the computed plots of streamline patterns corresponding to flow trapping mechanism associated with peristalsis. In order to track the relative trapping intensity, the computed velocity fields are numerically integrated to obtain estimates of the stream function according to Eqs. (12) and (13). The effect of the variation of $\bar{Q}/\pi ch^2$ on these three parameters are shown in Fig. 20(a)–(c) for selected values of $\alpha = 0.01$, 0.2 and 0.4 and for fixed $Re = 0.01$. The computational results of Takabatake *et al.* (1988) are superimposed for comparison. It can be seen that the present results are in good agreement with the their corresponding results when $\bar{Q}/\pi ch^2$ less than 0.5 while for $\bar{Q}/\pi ch^2 > 0.5$, results of Takabatake *et al.* (1988) are slightly higher than those computed by the present study. It also can be seen that the values of all the three parameters, i.e. (L_a/λ), $(L_b/H_{\max})$ and $|\psi_{\max}/\psi_{\text{wall}}|$ increase with increasing values of $\bar{Q}/\pi ch^2$. The corresponding variation of the computed streamlines for values of $\alpha = 0.2$ and 0.4 are shown in Figs. 21 and 22, respectively, and by comparing Figs. 18, 21 and 22, it can be observed that the variation of flow structure with mean flow rate is generally not influenced by the value of α, i.e. trapping area is increased with $\bar{Q}/\pi ch^2$ for all three cases. However, detailed comparison of Fig. 20(a)–(c) shows that there are significant differences for different α. These figures show that although the parameter (L_a/λ) increases with $\bar{Q}/\pi ch^2$ for the three values of α, the value of (L_a/λ) corresponding to the same value of $\bar{Q}/\pi ch^2$ decreases with α. Moreover, it can be seen that the values of $(L_b/H_{\max})$ exhibit no significant differences for three values of α. This is clearly reflected in the streamline figures that the size of the trapping region in the z direction decreases with α, while remaining relatively constant in the r direction. As can be seen from Fig. 20(c), the relative intensity $|\psi_{\max}/\psi_{\text{wall}}|$ shows no significant differences for the three values of α, when $\bar{Q}/\pi ch^2 < 0.6$, but shows an increasing trend with α when $\bar{Q}/\pi ch^2 > 0.6$. Trapping phenomena can occur only for certain combinations of $\bar{Q}/\pi ch^2$ and α. Figure 23shows the variation of computed onset value of trapping mean flow rate $\bar{Q}/\pi ch^2$ with α for $\varphi = 0.7$ and $Re = 0.01$. This figure basically shows the effect of α on the

value of onset trapping mean flow rate. It is clear that as α increases, the mean flow rate for the onset of trapping is significantly increased.

Trapping Corresponding to Re > 0.01

In order to investigate the trapping phenomena further, computations are done for higher Reynolds number, but for the same value of $\varphi = 0.7$ by varying α. The Reynolds number effect on $\bar{Q}/\pi ch^2$ at which the trapping onset takes place is shown in Fig. 24for $\alpha = 0.01$ and 0.2. It can be seen that for a fixed α, the increase of *Re* leads to a significant increase in $\bar{Q}/\pi ch^2$ which implies a delay in the onset of trapping. Figure 24 also shows that for $\alpha = 0.01$, there is a wide range of *Re* within which the trapping could occur. For the case corresponding to $\alpha = 0.2$, the

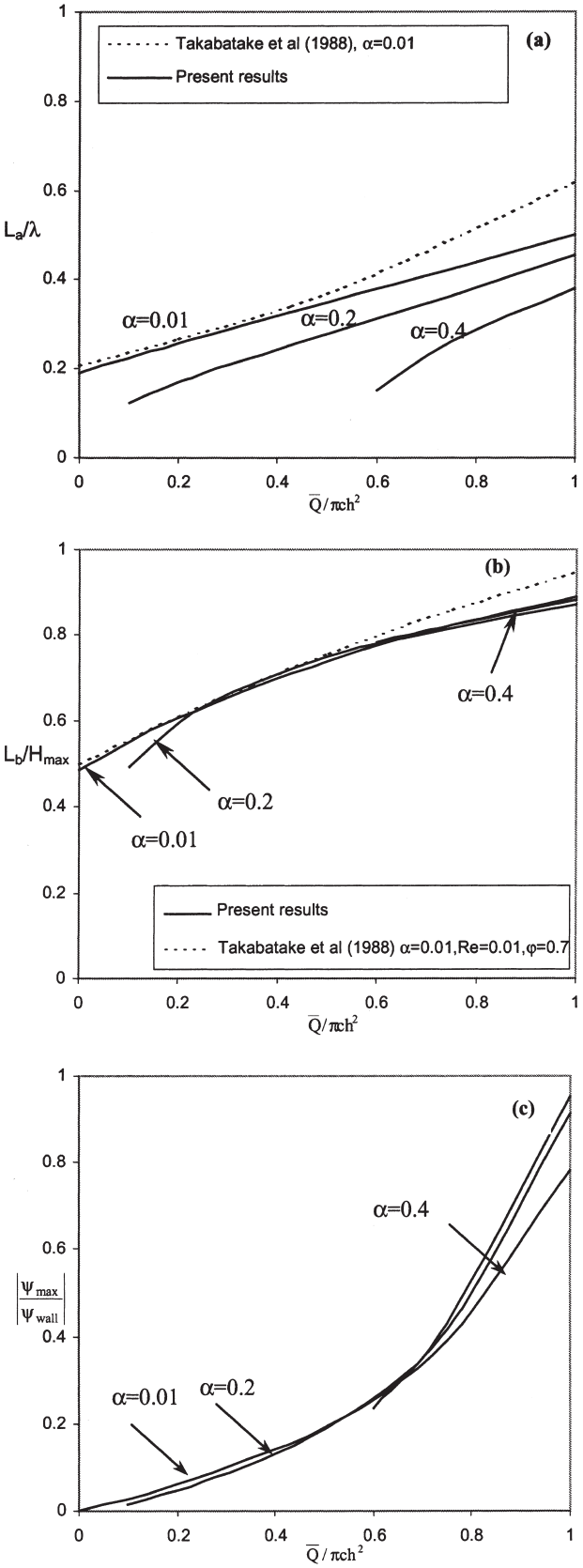

FIGURE 20 (a)–(c) The effect of $\bar{Q}/\pi ch^2$ on flow trapping mechanism for different values of α with $\varphi = 0.7$, $Re = 0.01$.

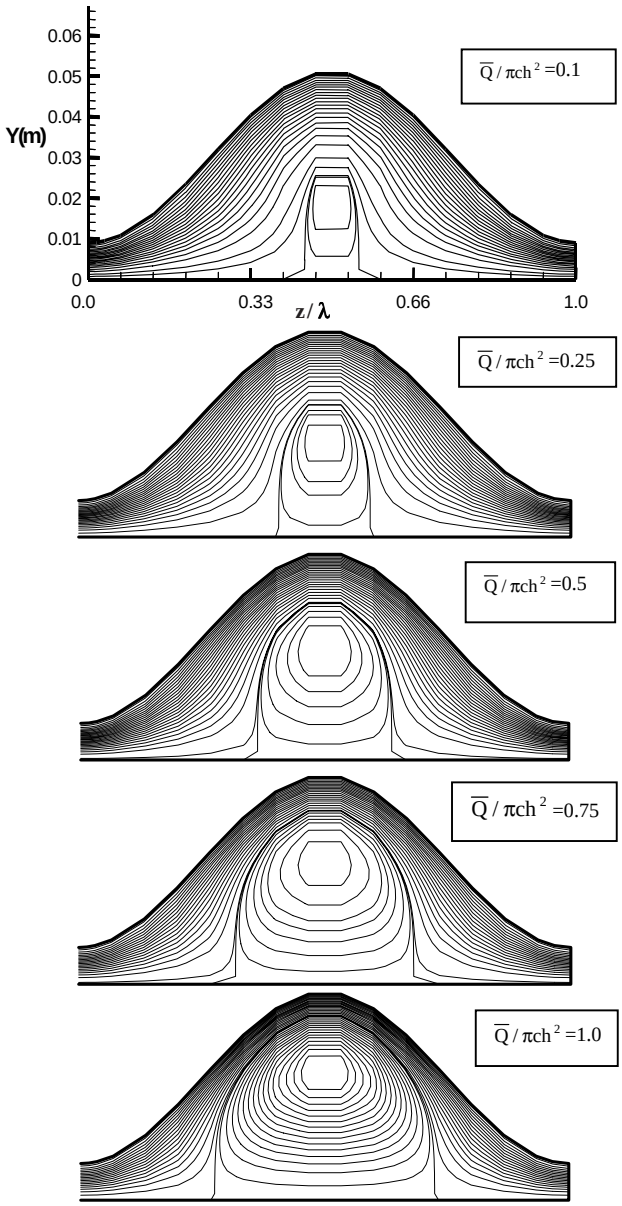

FIGURE 21 The streamline variation with $\bar{Q}/\pi ch^2$ (in the wave frame) for the case when $\varphi = 0.7$, $\alpha = 0.2$, $Re = 0.01$.

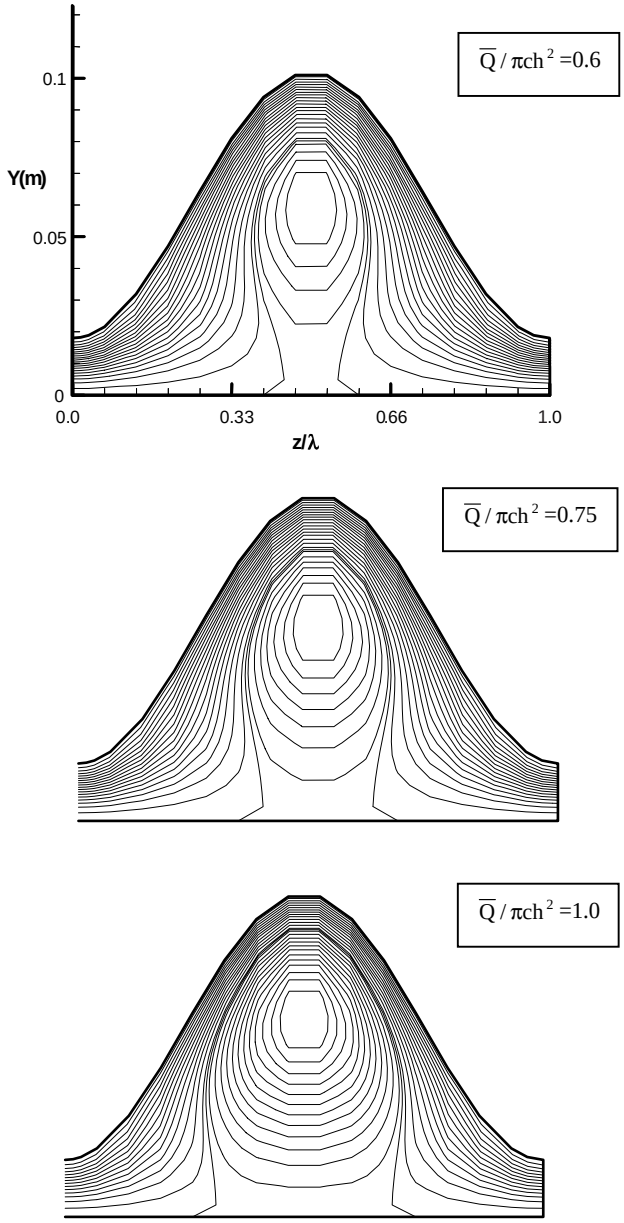

FIGURE 22 The streamline variation with $\bar{Q}/\pi ch^2$ (in the wave frame) for the case when $\varphi = 0.7$, $\alpha = 0.4$, $Re = 0.01$.

corresponding Reynolds number range is considerably decreased within 0.01–0.02 and for the case corresponding to $\alpha = 0.4$, it can be seen that trapping only occurs at $Re = 0.01$.

The variation of computed streamlines in the wave-frame with Reynolds number for the case corresponding to $\varphi = 0.7$, $\bar{Q}/\pi ch^2 = 0.6$, $\alpha = 0.2$ and $\alpha = 0.4$ are shown in Figs. 25 and 26, respectively. have been tracked during the course of the computation. The effect of the variation of $\bar{Q}/\pi ch^2$ on these three parameters trapping lengths (L_a/λ), $(L_b/H_{\max})$, and relative trapping intensity $|\psi_{\max}/\psi_{\text{wall}}|$ are quantitatively shown in Fig. 27(a)–(c).

By comparing these results with the results corresponding to $\alpha = 0.01$ shown in Fig. 6, the variation of computed streamlines show that for all the three cases, as Re increases, the trapping range decreases gradually and

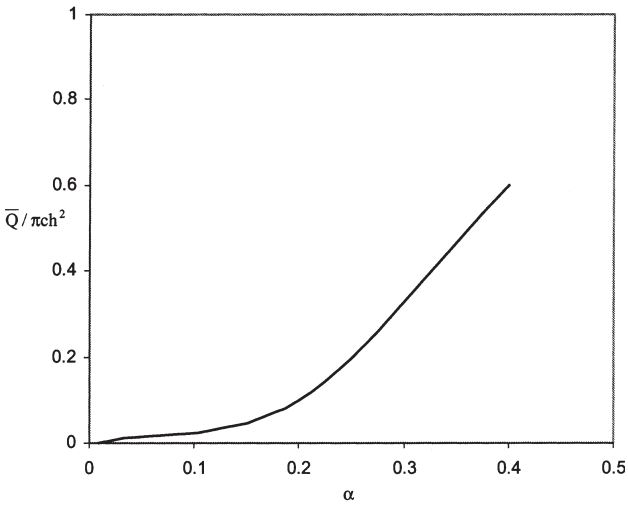

FIGURE 23 The effect of α on the onset trapping mean flow rate $\bar{Q}/\pi ch^2$ for the case when $\varphi = 0.7$ and $Re = 0.01$.

moves backward (in the direction of $-z$). Detailed analysis of Fig. 27(a)–(c) show that for a given α, the parameters (L_a/λ), $(L_b/H_{\max})$ and $|\psi_{\max}/\psi_{\text{wall}}|$ remain constant when $Re < 0.1$, but decreases sharply with Re when $Re > 0.1$. This implies that with the increase of intertial forces, the relative intensity of trapping decreases. For the same Reynolds number, the parameters (L_a/λ), $(L_b/H_{\max})$ and $|\psi_{\max}/\psi_{\text{wall}}|$ decrease with α.

CONCLUSIONS

In this work, peristaltic flow in an axi-symmetric tube has been simulated by solving the unsteady incompressible Navier–Stokes equations in primitive variables by the finite volume method. Compared with the previous theoretical methods used to study the peristaltic, the present method has no restrictions on the geometrical

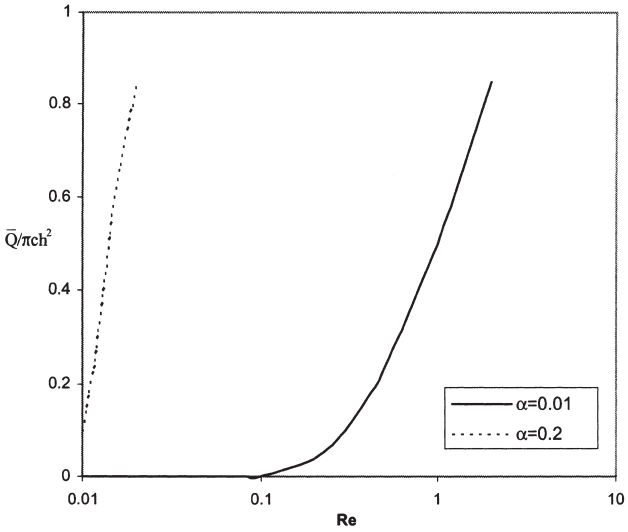

FIGURE 24 The effect of Reynolds number on the mean flow rate for the onset of trapping for the case when $\varphi = 0.7$.

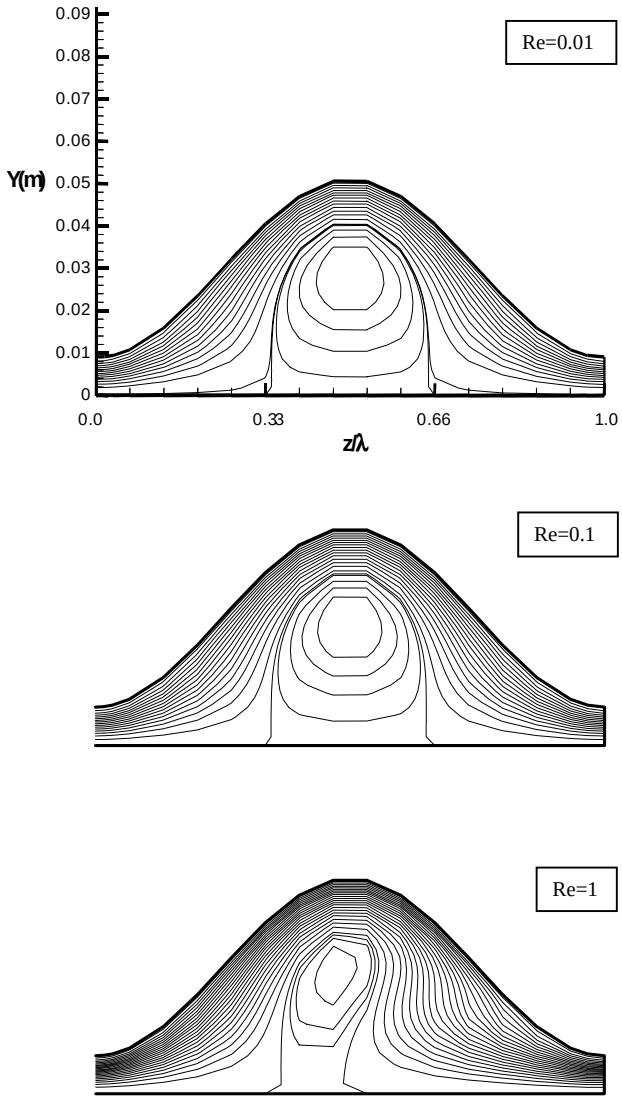

FIGURE 25 The streamline variation with Reynolds number (in the wave frame) for the case when $\varphi = 0.7$, $\alpha = 0.2$, and $\bar{Q}/\pi c h^2 = 0.6$.

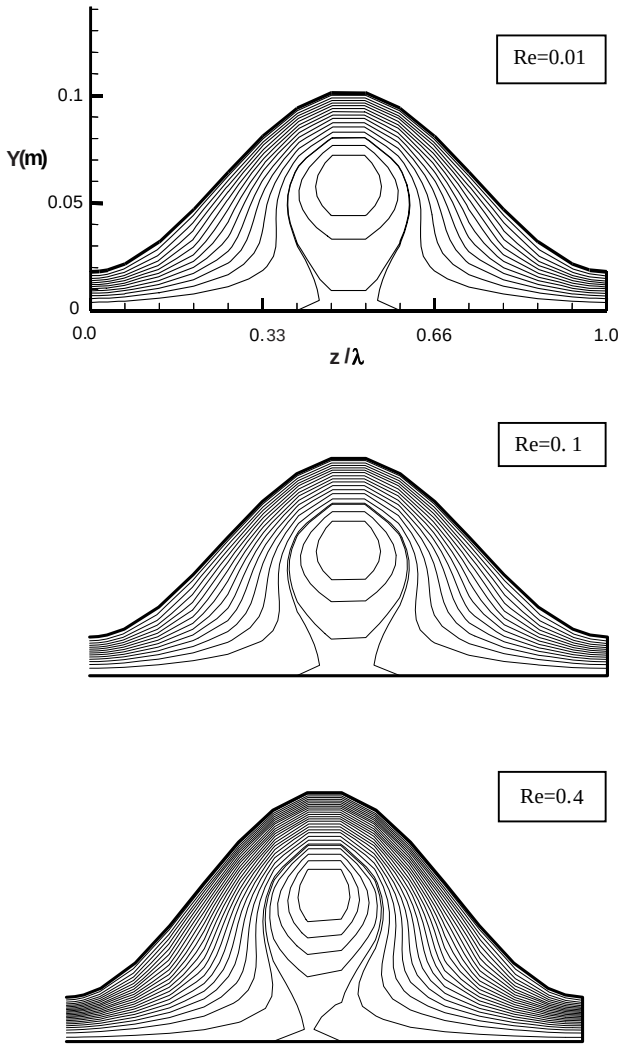

FIGURE 26 The streamline variation with Reynolds number (in the wave frame) for the case when $\varphi = 0.7$, $\alpha = 0.4$, and $\bar{Q}/\pi c h^2 = 0.6$.

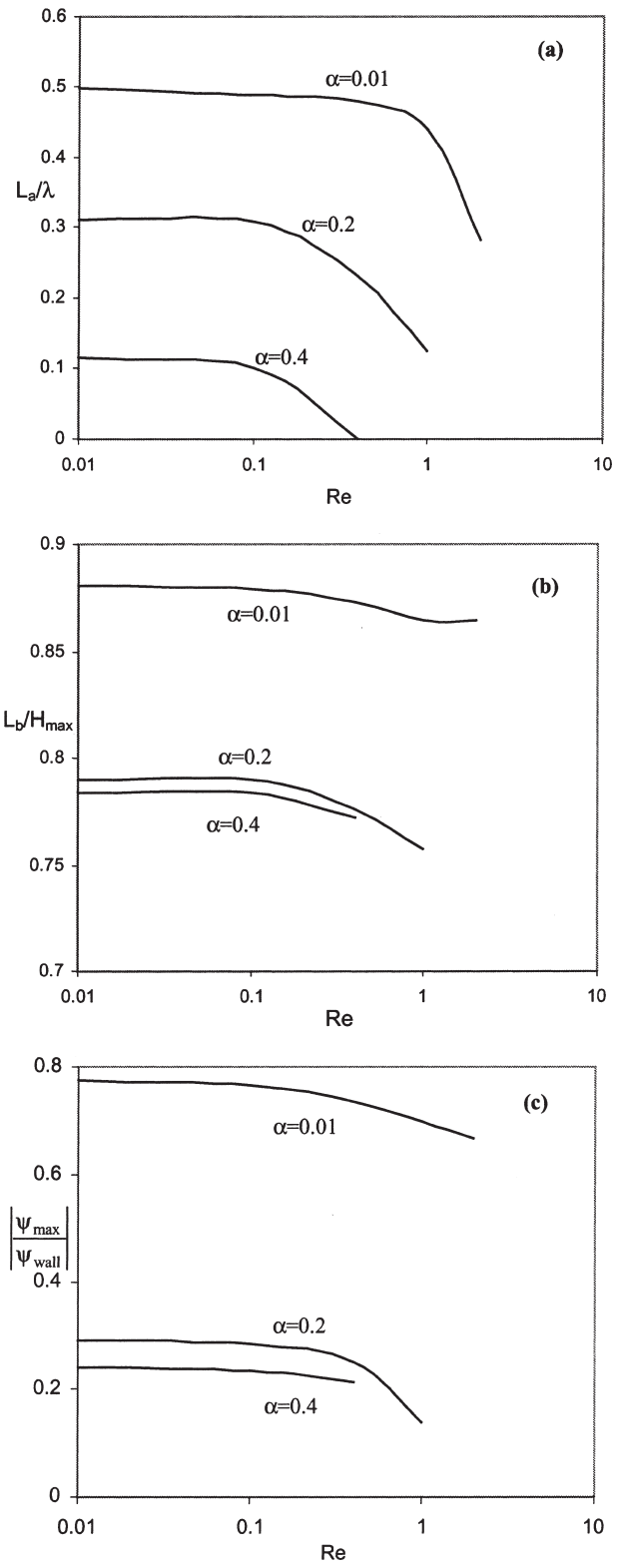

FIGURE 27 The Reynolds number effect on the (a) $(L_a/\lambda)-Re$ variation (b) $(L_a/H_{\max})-Re$ variation (c) $|\psi_{\max}/\psi_{\text{wall}}|-Re$ variation for the case when $\varphi = 0.7$, $\bar{Q}/\pi ch^2 = 0.6$ for different values of α.

shape of the walls (α, φ). The numerical method used here has no restriction on the range of Reynolds number defined for peristalsis and hence can be used to simulated peristalsis for a much wider range of Reynolds number. With regard to the flow trapping phenomena, which results from peristalsis, the present study has also been extended to a much wider range of wave numbers than those reported in literature, and more quantitative results are presented for the trapping. From the computed unsteady peristaltic flow fields, systematic analysis of the effect of Reynolds number and wavelength and wave amplitude on the velocity fields, pressure and shear stress distribution associated with peristalsis have also been extracted to provide useful insight into the operation of the peristaltic pump at higher Reynolds number.

References

Brown, T.D. and Hung, T.K. (1977) "Computational and experimental investigations of two-dimensional nonlinear peristaltic flows", *J. Fluid Mech.* **83**, (part 2), 249–272.

Fung, Y.C. and Yih, C.S. (1968) "Peristaltic transport", *Trans. ASME J. Appl. Mech.* **35**, 669–675.

Jaffrin, M.Y. (1973) "Internal and streamline curvature effects on peristaltic pumping", *Int. J. Eng. Sci.* **11**, 681–699.

Jaffrin, M.Y. and Shapiro, A.H. (1971) "Peristaltic pumping", *Ann. Rev. Fluid Mech.* **3**, 13–36.

Pozrikids (1987) "A study of peristaltic flow", *J. Fluid Mech.* **180**, 515–527.

Rathish, B.V. and Naidu, K.B. (1995) "A numerical study of peristaltic flows", *Comput. Fluids* **24**, 161–176.

Shapiro, A.H., Jaffrin, M.Y. and Weinberg, S.L. (1969) "Peristaltic pumping with long wave-lengths at low Reynolds numbers", *J. Fluid Mech.* **37**, 799–825.

Takabatake, S. and Ayukawa, K. (1982) "Numerical study of two-dimensional peristaltic flows", *J. Fluid Mech.* **122**, 439–465.

Takabatake, S., Ayukawa, K. and Mori, A. (1988) "Peristaltic pumping in circular cylindrical tubes: a numerical study of fluid transport and its efficiency", *J. Fluid Mech.* **193**, 267–283.

Yin, F. and Fung, Y.C. (1969) "Peristaltic waves in circular cylindrical tubes", *Trans. ASME E: J. Appl. Mech.* **36**, 579–587.